optica

Diffraction tomography with Fourier ptychography: supplementary material

ROARKE HORSTMEYER[1,2,*], JAEBUM CHUNG[1], XIAOZE OU[1], GUOAN ZHENG[3], AND CHANGHUEI YANG[1]

[1] Department of Electrical Engineering, California Institute of Technology, Pasadena, California 91125, USA
[2] Bioimaging and Neurophotonics Lab, NeuroCure Cluster of Excellence, Charité Berlin, Humboldt University, Berlin 10117, Germany
[3] Department of Biomedical Engineering, University of Connecticut, Storrs, Connecticut 06269, USA
[*] Corresponding author: roarke@caltech.edu

Published 27 July 2016

This document provides supplementary information for "Diffraction tomography with Fourier ptychography," http://dx.doi.org/10.1364/optica.3.000827. It analyzes the convergence of the Fourier ptychographic tomography (FPT) algorithm in the presence of noise, then examines the connection between the first Born approximation and the multi-slice model, and finally includes additional experimental results for a sample that does not obey the first Born condition.

http://dx.doi.org/10.1364/optica.3.000827.s001

1. ALGORITHM CONVERGENCE

In this section, we examine the convergence of the FPT algorithm in simulation. We test two different samples that follow the first Born approximation. As discussed in the main text, a sample obeys the first Born approximation when it is valid to substitute the scattered field within the sample, $U(\mathbf{r}) = U_i(\mathbf{r}) + U_s(\mathbf{r})$, with the incident field, $U_i(\mathbf{r})$. This requires the inequality $U_i(\mathbf{r}) \gg U_s(\mathbf{r})$. As detailed in [1], this inequality leads to the approximate first Born condition in the main text,

$$kt\,|\Delta n|\,/2 \ll 1, \tag{S1}$$

where $\Delta n = n(\mathbf{r}) - n_b$, t is the sample thickness, k is the wavenumber in vacuum and the background medium index of refraction is n_b.

Our first simulated sample consists of several transparent microspheres, each with a maximum index of refraction $n = 1.505$ and a 7 μm diameter, that are immersed in oil with background index $n_b = 1.5$ (see Fig. S1(a)). We note that these simulated beads approximately obey the above first Born condition ($kt\Delta n/2 \approx 0.2$). For simplicity and ease of visualization, our simulations here are in two dimensions along (x, z). We expect our findings to easily generalize to the 3D case.

Similar to our experimental system, the simulated microscope has an objective numerical aperture (NA) of 0.4 and an illumination NA of 0.4. We simulate 64 intensity images, generated from 64 individual LEDs that emit quasi-monochromatic light (central wavelength $\lambda = 0.5\mu$m), with each 1D image containing 200 pixels that sample the field at the Nyquist-Shannon limit. An example reconstruction is shown in Fig. S1(c). The FPT algorithm here uses light field initialization, similar to reconstructions in the main text.

The convergence of the FPT algorithm in the presence of noise is shown in Fig. S1(d). First, we show the reconstruction mean squared error (MSE), which we define as,

$$E_M = \frac{\sum_{(x,z)} |\psi(x,z) - \gamma v(x,z)|^2}{\sum_{(x,z)} |\psi(x,z)|^2}. \tag{S2}$$

Here, ψ is the reconstructed scattering potential and $v(x,z)$ is the ideal scattering potential that our microscope could reconstruct if it could directly measure phase and then perform standard diffraction tomography with the measured complex fields (as shown in Fig. S1(b)). Put another way, we compute the MSE by only considering values of the sample and reconstruction that fall within the limited k-space bandpass of the FPT system, and do not consider values that fall outside of this finite bandpass (where we assume our setup cannot measure anything). The parameter γ is a constant phase factor that shifts our reconstructed scattering potential phase to optimally match the ground truth phase:

$$\gamma = \frac{\sum_{(x,z)} \psi(x,z) v^*(x,z)}{\sum_{(x,z)} |v(x,z)|^2}, \tag{S3}$$

We also add Gaussian noise to each simulated intensity image. We summarize the amount of noise with a signal-to-noise ratio

(SNR) defined as,

$$SNR = 10\log_{10}\left(\frac{\langle I\rangle}{\langle N\rangle}\right), \quad \textbf{(S4)}$$

where $\langle I\rangle$ is the mean intensity over all images and $\langle N\rangle$ is the mean intensity of the uncorrelated Gaussian noise added to each simulated image. We show example convergence plots for 4 levels of noise, ranging from a high amount of noise (SNR=13 dB) to a relatively low amount (SNR = 30 dB).

At the bottom of Fig. S1(d), we also plot the peak signal-to-noise ratio (PSNR) as a function of iteration. PSNR is defined as,

$$PSNR = 10\log_{10}\left(\frac{\max(|V|)^2}{\hat{E}_M}\right), \quad \textbf{(S5)}$$

where $\hat{E}_M = \frac{1}{N}E_M$ and N is the number of reconstruction pixels. Convergence of the algorithm is quite clear across the 4 tested noise levels. Remaining error is likely caused by the finite amount of added noise, an imperfect degree of overlap at some k-space pixels, and possible misalignments in the light field initialization.

Second, we simulate a similar sample with both real and imaginary variations in its index of refraction (i.e., the microspheres also absorb light). In the example in Fig. S2, each of the 12 microspheres has a maximum index shift of Re(Δn)=.005 and Im(Δn)=.01, where this latter imaginary index shift indicates absorption. The plots in Fig. S2(d) demonstrate that FPT still successfully converges in the presence of absorption.

2. SIMULATING FPT WITH THE MULTI-SLICE MODEL

In this section, we briefly connect FPT (operating under the first Born approximation) to the multi-slice model as used in [2] and [3]. First, we use each model to simulate microscope images of a relatively thin and weakly scattering sample that we expect to obey both the first Born and multi-slice approximations. Then, we perform FPT using the two distinct image sets, allowing us to compare the performance of FPT under the two unique forward models. We first demonstrate that for a weakly scattering sample, each approximation leads to a roughly equivalent reconstruction. Second, we use the multi-slice model to simulate images from a sample that does not meet the first Born criterion, and once again we achieve an accurate FPT reconstruction using these multi-slice images as input, which highlights algorithm robustness.

Here are the steps for our first FPT-multi-slice comparison in Fig. S3. First, we define an example index of refraction map $n(x,z)$ that contains three microspheres of different sizes (with diameters $t = 6$, 12 and 25 μm), each exhibiting the same shift in index of refraction (Re(Δn)=.001 and Im(Δn)=.001). The real part of this index is shown in Fig. S3(a). All three of these spheres obey the first Born condition.The total sample size is 300 μm wide and 125 μm thick.

Second, we compute the associated k-space scattering potential $\hat{v}(k_x,k_z)$ and sample this function to create a set of optical fields that lead to "FPT images", $g_{FPT}(x,j)$, following Eq. 6 in the main text. Here, $1 \le j \le q$ again denotes the jth plane wave angle, leading to $q = 64$ uniquely illuminated images. The FPT image set, g_{FPT}, is displayed in Fig. S3(c) (after subtraction of the illumination field) and it implicitly assumes the validity of first Born approximation. The simulated system here matches the specifications described above ($NA_o = 0.4$, $NA_i = 0.4$) and includes independent Gaussian noise.

Third, we use the same index of refraction map for multi-slice simulation. Here, we propagate $q = 64$ plane waves with the same angles through the same sample index of refraction map, but now propagation proceeds one slice at a time. At each discretized slice z_d, we assume that $n(x,z_d)$ acts as an infinitely thin phase plate with an absorption profile $\exp(-ktn_{im}(x,z_d))$ and phase shift profile $\exp(-ktn_r(x,z_d))$. Between slices, we assume free space propagation. After propagating the incident field through the entire sample, we then refocus the scattered fields to the center of the sample and subsequently simulate image formation through the limited numerical aperture objective focused at this central plane. This creates a second image set, $g_{MS}(x,j)$, which we display in Fig. S3(e). All steps, including the propagation kernel and method of image formation, follow from the techniques presented in [2].

Finally, we perform FPT reconstruction using each image set, g_{FPT} and g_{MS}, as separate inputs. The results after 10 iterations (using SNR=20 dB) are shown in Fig. S3(d) and (f), respectively. The two reconstructions match quite closely, as expected given that the two detected image sets shown in Fig. S3(c) and (e) are quite similar.

For our second FPT-multi-slice comparison, we again use the multi-slice method to create uniquely illuminated images of a thick sample and perform FPT, but now with a sample that does *not* obey the first Born condition (see Fig. S4(a)). The index shift for each sphere is higher (Re(Δn)=.01 and Im(Δn)=.01), the sphere diameters are again $t = 6$, 12 and 25 μm and there are more spheres that may lead to multiple scattering. The reconstruction in Fig. S4(d) using $q = 128$ images is not as accurate as the prior example in Fig. S3. However, this example demonstrates that FPT, using multi-slice images, can still successfully recover the approximate size, location and refractive index shift of each sphere, even when they do not obey the first Born condition and the effects of multiple scattering are present. Future work will attempt to improve the quality of the reconstruction in (d) by taking into account multiple-scattered light.

3. RECONSTRUCTING SAMPLES THAT DO NOT OBEY THE FIRST BORN APPROXIMATION

Fig. S5 presents an experimental FPT reconstruction of a sample that does not obey the first Born condition: a large pollen grain immersed in oil. The grain dimensions are approximately 50 μm thick and 125 x 50 μm wide along x and y. As is clear in the raw images in Fig. S5(a), the pollen grain is quite absorptive. As we vary the focus for our raw images, the overall brightness across the sample remains low, leading us to conclude that these low intensities are not caused by interference alone. Even without considering the effects of sample absorption, we do not expect this sample to follow the first Born condition. If we estimate the thickness of the pollen grain at 50 μm (from manual focusing), assume the background material is Kleermount and Xylene with an index of refraction $n_b = 1.52$, and also assume the index of refraction of the pollen grain matches previous studies [4] as approximately $n = 1.53$, then from Eq S1 we find that $kt\Delta n/2 = 2.5$.

FPT reconstructions of this pollen grain are in Fig. S5(b), where we use the same data capture and processing steps as outlined in the main text. We display 3 separate slices of the real component of the recovered refractive index. This may be compared with the corresponding light field reconstruction, where each image has been refocused to the same axial plane, in Fig. S5(c), as well as the raw refocused images in Fig. S5(a).

FPT recovers the general shape of the grain and different structures within each slice, although it is not clear if the large variations within the middle slices accurately match the internal structure of the sample. FPT also still reveals several features that are not present within the raw images or the light field reconstruction. Since the total optical path through the grain at its edges (i.e., along the grain wall in Fig. S5) remains relatively short, we expect minimal sample absorption and phase shift here. Thus, we expect these wall regions to more closely satisfy the first Born condition. At these edge locations, we observe (especially within the middle FPT slice) that the pollen grain wall is roughly patterned. This roughness is consistent with the commonly observed patterning of the exine layer of pollen grains. The high-resolution patterning is missing or not resolved within the raw and light field images.

REFERENCES

1. B. Chen and J. J. Stamnes, "Validity of diffraction tomography based on the first Born and the first Rytov approximations," Appl. Opt **37**, 2996–3006 (1998).
2. L. Tian and L. Waller, "3D intensity and phase imaging from light field measurements in an LED array microscope," Optica **2**, 104–111 (2015).
3. P. Li, D. J. Batey, T. B. Edo and J. M. Rodenburg, "Separation of three-dimensional scattering effects in tilt-series Fourier ptychography," Ultramicroscopy **158**, 1–7 (2015).
4. F. Charrière, A. Marian, F. Montfort, J. Kuehn T. Colomb, E. Cuche, P. Marquet and C. Depeursinge, "Cell refractive index tomography by digital holographic microscopy," Opt. Lett. **2**, 178–180 (2006).

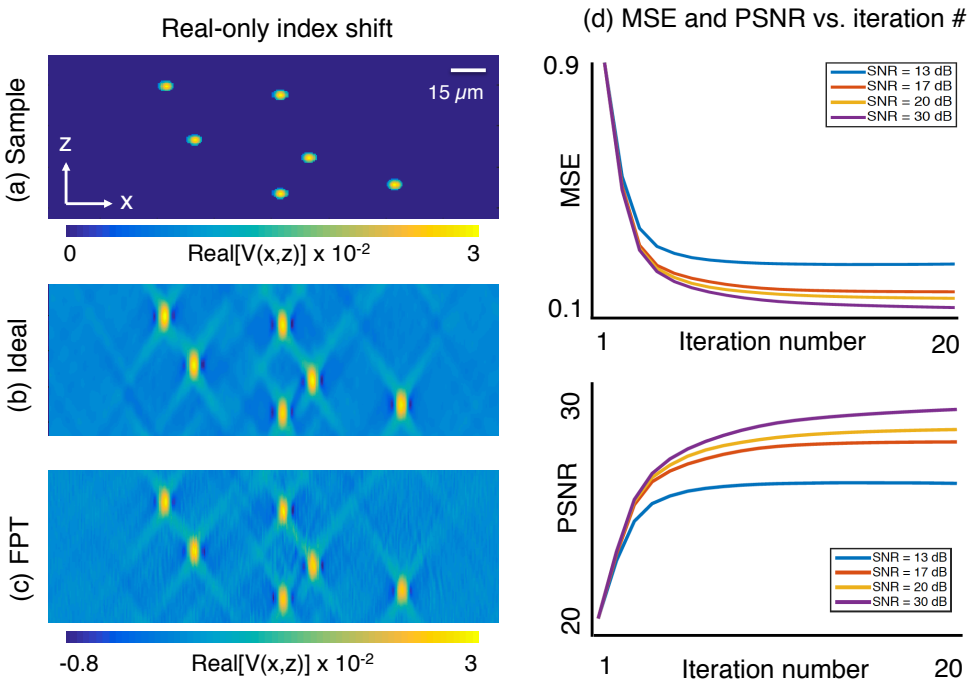

Fig. S1. FPT simulation of a 2D set of non-absorbing microspheres that satisfy the first Born condition. (a) The real component of the scattering potential. (b) The ideally recovered scattering potential, created by filtering the complex k-space scattering potential with the simulated microscope's limited bandpass ($NA_o = 0.4$, $NA_i = 0.4$). (c) The FPT reconstruction with SNR = 20 dB. (d) MSE and PSNR between the ideal and FPT reconstructions as a function of iteration number for 4 levels of SNR.

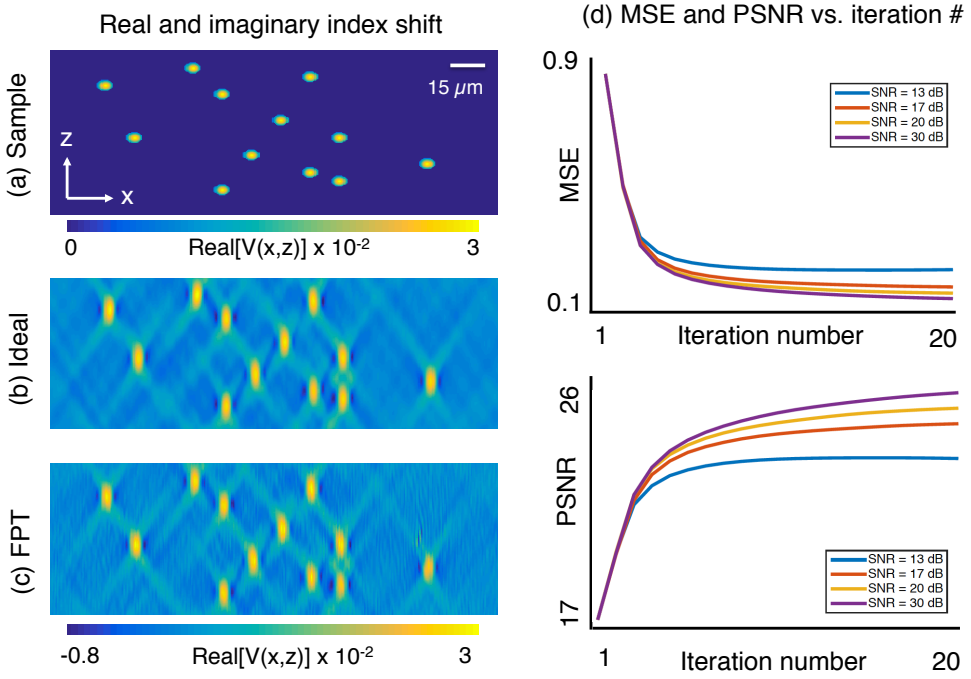

Fig. S2. FPT simulation following the same outline as Fig. S1. (a) The imaged microspheres (with Re(Δn)=.005 and Im(Δn)=.01) now also absorbs light. (b) Ideal reconstruction, (c) FPT reconstruction and (d) MSE and PSNR plots across different noise levels showing algorithm convergence.

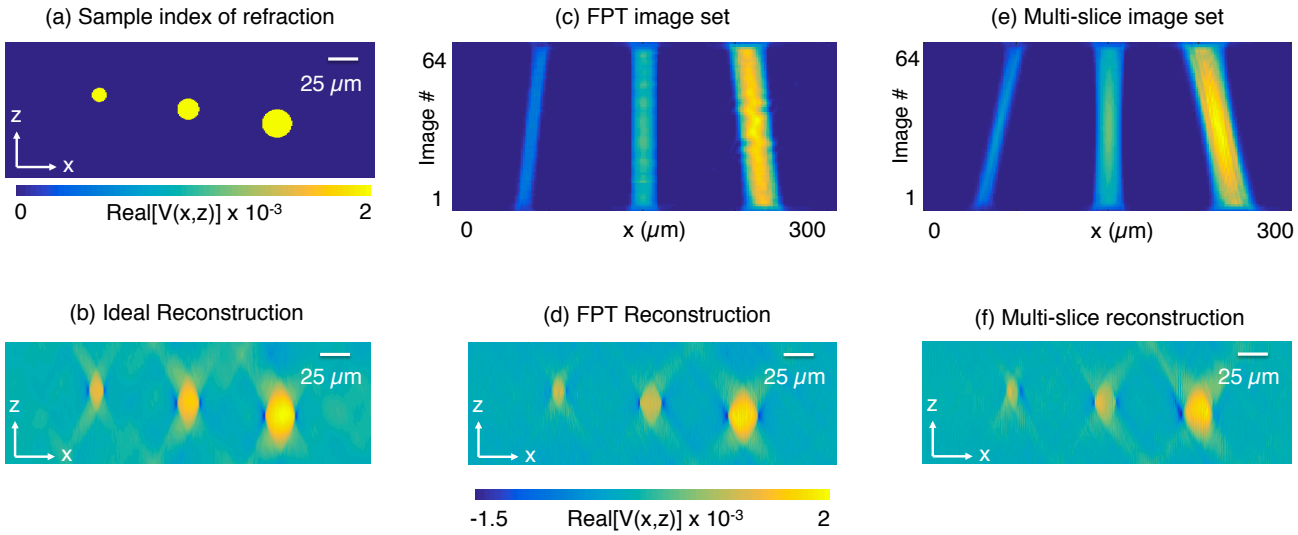

Fig. S3. FPT and multi-slice simulation: sample obeys first Born condition. (a) Real part of scattering potential includes three different sized spheres at slightly different depth planes. (b) Ideal reconstruction expected by DT for a microscope system with $\mathrm{NA}_o = 0.4, \mathrm{NA}_i = 0.4$. (c) Image set generated by FPT forward model. Each image is the squared Fourier transform of one arc of the scattering potential. (d) Resulting FPT reconstruction using the image set in (c) as algorithm input. (e) Image set created by multi-slice propagation. Each plane of the index of refraction is treated as a thin amplitude and phase plane. (f) The resulting FPT reconstruction using the image set in (e) as algorithm input. For this simple sample, FPT and multi-slice image sets and reconstructions match.

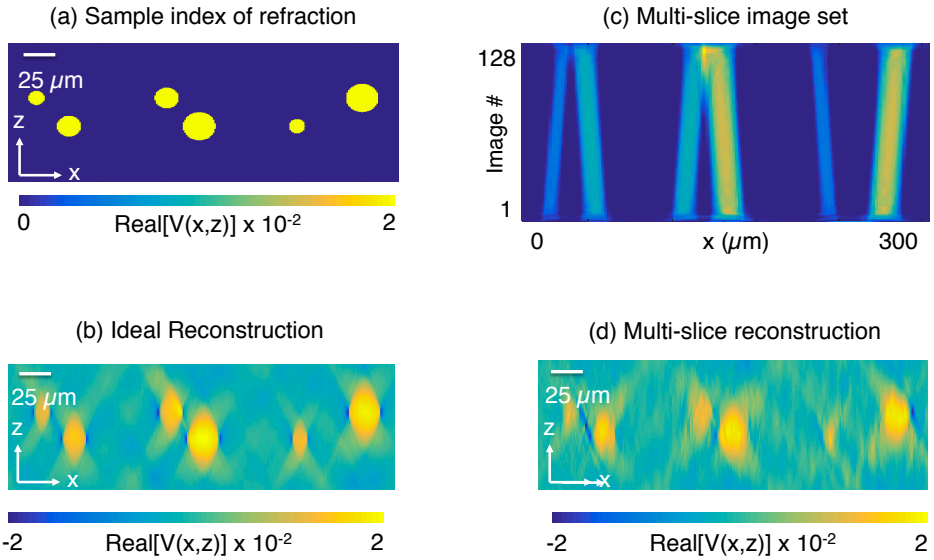

Fig. S4. FPT and multi-slice simulation: sample does not obey the first Born condition. (a) Real part of sample scattering potential shows 6 different spheres at different depths. (b) The ideal reconstruction expected using the same microscope as in Fig S3(b). (c) Multi-slice image set. (d) FPT reconstruction using the multi-slice generated image set in (c), where each sphere is resolved.

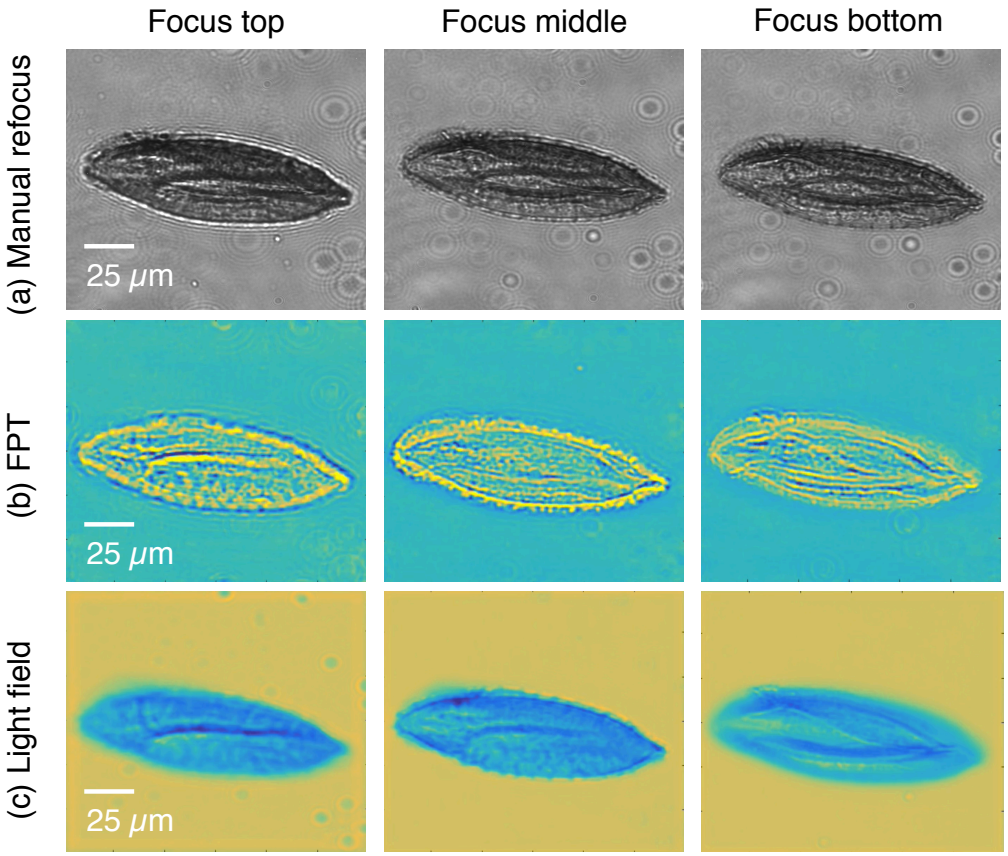

Fig. S5. FPT reconstruction of a pollen grain. This thick sample significantly absorbs and phase-shifts incident light. Thus, it does not follow the first Born condition. (a) Raw refocused images, (b) the FPT reconstruction and (c) slices of the refocused light field are included at three different axial slices. We note that the axial slice location of the manual refocused images only roughly approximates the slice locations of the FPT and light field reconstructions.